ASCE

Full-Scale Test of a Steel–Concrete Composite Floor System with Moment-Resisting Connections under a Middle-Edge Column Removal Scenario

Junjie Wang[1]; Wei Wang, M.ASCE[2]; and Yihai Bao, P.E., M.ASCE[3]

Abstract: To investigate the load-resisting mechanisms and responses of typical steel–concrete composite frames under the progressive collapse scenario, a 2 × 1 bay full-scale steel–concrete composite floor system was quasi-statically tested till failure under a middle-edge column removal scenario. The test specimen was extracted from a prototype building, which was designed according to modern design codes. Based on the measured load-deflection response, load-carrying mechanisms, deformation patterns, and failure modes were discussed in detail. The maximum capacity was achieved at a chord rotation angle of 0.163 rad, where the steel girder and the composite slab contributed 19.2% and 80.8% of the total resistance, respectively. The peak resistant load, as a result of the combined catenary and tensile membrane action, is 15.9% higher than that of the flexural action alone. The load-carrying capacity of the test specimen is 5.5 times larger than the ASCE load combination for extraordinary events. The continuous steel deck and moment-resisting beam–column connections have a significant influence on the load-carrying capacity and the deformation capacity of the composite floor system. **DOI: 10.1061/(ASCE)ST.1943-541X.0002630.**

Author keywords: Progressive collapse; Disproportionate collapse; Membrane action; Catenary action; Composite slab; Steel beam–column connection.

Introduction

Progressive collapse of structures starts with the failure of a few structural elements, such as columns and/or beam–column connections, and then passes to adjacent elements or even the whole of a structure (Starossek 2009). Potential causes of progressive collapse include design and construction flaws or extreme events such as fire, gas explosions, and bomb attacks. Considering the catastrophic consequences of progressive collapse, several design and strengthening methods are proposed in some design guidelines, including the General Services Administration guidelines (GSA 2013), Unified Facilities Criteria (DoD 2016), ASCE/SEI 7-16 (ASCE 2017), and EN 1991-1-7 (CEN 2006). In these documents, the progressive collapse resistance of structures is analyzed by calculating the robustness of the residual structures after removing critical columns. In order to prevent collapse, the load initially carried by the removed column needs to be redistributed to the rest of the structural members through alternative load paths.

As the development pace of computational capacity and simulation techniques increases, the numerical approach becomes a viable alternative for researchers and engineers to solve structural problems. However, considering the excessive nonlinearity and severe damage of structures under the progressive collapse scenario, high-quality experimental data are vital to the validation of numerical results. According to Li et al. (2017), the experimental tests can be categorized into three different levels: (1) the subassemblage test, (2) the one-story floor system test, and (3) the full structural system test. The one-story floor system test is considered to be the most efficient and balanced in terms of complexity and cost. Many researchers have studied progressive collapse behaviors of floor systems via the numerical approach. Sadek et al. (2008) computationally studied the robustness of a gravity steel frame with a composite slab in the event that a center column was removed. The results have shown that the steel deck could significantly improve the load-carrying capacity of composite floor systems. Alashker et al. (2010, 2011) conducted a series of simulations to investigate the influence of key parameters, such as steel deck thickness, steel reinforcement ratio, and shear-tab connection strength, on the robustness of composite floors subjected to the removal of a center column. The study showed that the main collapse resistance came from the steel deck and suggested that only the three-dimensional models could accurately reflect the complex collapse behavior of composite floor systems. Furthermore, an iterative design method was proposed later based on the simulations (Alashker and El-Tawil 2011). Li et al. (2013) compared different simplified approximations of collapse modeling and found that the planar models tended to underestimate the robustness of the studied structure because the contribution of the slab was not taken into account. Elsanadedy et al. (2014) simulated the progressive collapse of a typical multistory framed building caused by an accidental blast, in which a simplified two-stage nonlinear dynamic analysis method was proposed. Bao et al. (2017) conducted a series of push-down analyses of a 10-story reinforced concrete frame building and pointed out that the results generated from the one-story floor simulation may overestimate the structural robustness

[1]Ph.D. Candidate, State Key Laboratory of Disaster Reduction in Civil Engineering and Dept. of Structural Engineering, Tongji Univ., Shanghai 200092, China. ORCID: https://orcid.org/0000-0002-3397-2813. Email: 1991wang@tongji.edu.cn

[2]Professor, State Key Laboratory of Disaster Reduction in Civil Engineering and Dept. of Structural Engineering, Tongji Univ., Shanghai 200092, China (corresponding author). ORCID: https://orcid.org/0000-0003-1241-465X. Email: weiwang@tongji.edu.cn

[3]Independent Consultant Engineer, Gaithersburg, MD 20878. Email: baoyihai@gmail.com

Note. This manuscript was submitted on September 7, 2018; approved on November 1, 2019; published online on March 5, 2020. Discussion period open until August 5, 2020; separate discussions must be submitted for individual papers. This paper is part of the ***Journal of Structural Engineering***, © ASCE, ISSN 0733-9445.

as the ground-floor columns would result in a premature instability for relatively high buildings.

In recent years, several experimental studies on floor systems have been reported in the literature. Johnson et al. (2015) tested a half-scale one-story composite floor system subjected to internal, edge, and corner column removals. The tested substructure was extracted from the gravity frames of a typical commercial building without any special enhancement for progressive collapse. Even though the composite slab contributed significantly to the vertical resistance, all test specimens could not sustain the design load combination. Hadjioannou et al. (2013, 2018) conducted a similar test to that by Johnson et al. (2015), except that a stronger horizontal boundary condition and a thicker slab were adopted in the test conducted by Hadjioannou et al. (2018). Two specimens were tested under the internal-column removal scenario and the edge-column removal scenario, respectively. Both specimens survived under the design load combination. Furthermore, the composite slab could solely sustain the design load combination with all bolts connected to the damaged column being removed. As indicated by these studies, the boundary condition significantly affects the load-carrying capacity of composite floor systems. Fu et al. (2017) investigated the collapse behavior of a one-third scale composite floor system with semirigid beam–column connections. The contribution of the composite slab and steel beams was quantified, where the composite slab could sustain at least one-third of the total vertical load. The collapse behavior of concrete floor systems has also been experimentally studied by Qian and Li (2012), Qian et al. (2014, 2016), Dat and Tan (2014), Lu et al. (2017), and Lim et al. (2017).

In all the aforementioned experimental studies, reduced-scale specimens were tested. Although the results obtained from the reduced-scale specimens could provide useful insights on structural responses to some extent, they may not be able to accurately reflect the actual behaviors of the prototype structures. Harris and Sabnis (1999) noted that the only practical way to model the realistic behaviors of reinforced concrete structures is to use the same concrete material as the prototype structure, and at the same time, all the geometric dimensions must be scaled with the same factor. As described by Johnson et al. (2015), even if it was just a half-scale model, it was hard to find the desirable steel members to meet the geometrical scale requirement at every location. For example, it is difficult to find a 0.6-mm steel deck for a half-scale specimen from the prototype structure with a steel deck 1.2 mm in thickness, because the typical thickness of a profiled steel deck is between 0.8 and 1.2 mm. Furthermore, the smooth wire in small-scale specimens has different bond behavior compared to that of the deformed bar in the prototype structure. Considering the limitations of reduced-scale specimens, it would be desirable to conduct full-scale experimental studies.

Compared with interior columns, peripheral columns are more likely to be affected during the extreme event. Moreover, the load-distribution paths under a peripheral-column removal case are relatively limited compared to those under an interior-column removal case. A building with a regular column spacing and structure layout would have a good chance of surviving under the interior-column removal if it could withstand the peripheral-column removal. In this study, a middle-edge column loss scenario is adopted, which is considered a relatively unfavorable situation due to the peripheral-column removal and the partially developed membrane action. As suggested by Sadek et al. (2008), Johnson et al. (2015), and Hadjioannou et al. (2018), the moment connection and the continuity of the steel deck are two factors that could improve the load-carrying capacity under progressive collapse scenarios. Therefore, a full-scale composite floor with a continuous steel deck and rigid beam–column connections has been designed in this study to investigate the realistic behaviors of composite floor systems under an edge-column removal scenario.

The primary objective of this research is to study the performance of a typical composite floor system under a middle-edge column loss scenario, including the load-deflection response, load-carrying mechanisms, deformation patterns, and failure modes. In addition, the experimental data generated from this test can be used to validate numerical models, which are crucial for future parametric studies.

Experimental Program

Prototype Structure

In order to reflect the realistic performance of a typical composite floor system, a 4×4 bay five-story steel–concrete composite frame structure (Fig. 1) has been designed according to the Chinese building codes [GB50017 (MOHURD 2003); GB50011 (MOHURD 2010)]. The basic design concept is similar between the Chinese building codes and the American building codes [AISC 360 (AISC 2010); ASCE/SEI 7-16 (ASCE 2017)], except that a typical steel building in China is usually designed with moment-resisting frames, and beams and columns are connected with rigid joints. This prototype building is designed as an apartment building, therefore relatively smaller span lengths, 4.2 m for girder span and 3.6 m for beam span, are adopted. The story height of the prototype building is 3.6 m. The design dead load (DL) is 5 kN/m^2 and the live load (LL) is 2 kN/m^2. The designed basic earthquake acceleration

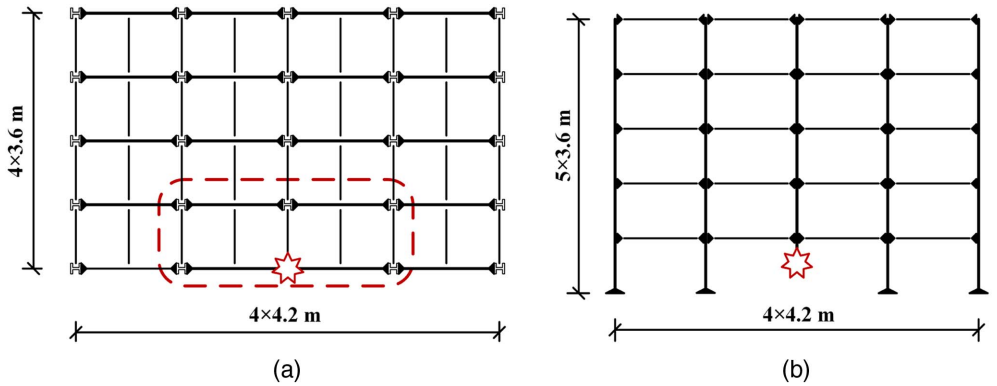

Fig. 1. Prototype structure: (a) plan view; and (b) elevation view.

J. Struct. Eng., 2020, 146(5): 04020067

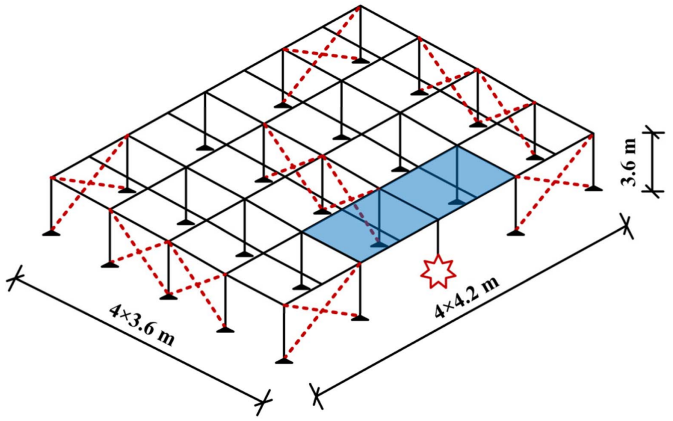

Fig. 2. Layout of steel brace.

Table 1. Geometrical dimensions of structural elements (in millimeters)

Structural elements	$H \times B \times t_w \times t_f$
Girder	H200 × 100 × 5.5 × 8
Beam	H150 × 75 × 7 × 10
Column	H200 × 200 × 8 × 12
Brace	H100 × 100 × 6 × 8

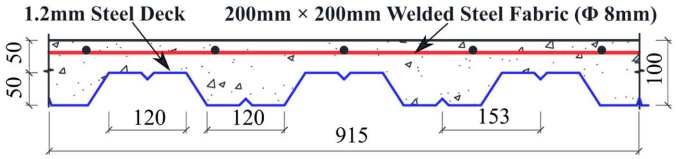

Fig. 3. Dimensions of slab.

is 0.1g and the designed basic wind pressure is 0.55 kN/m^2. Lateral loads are resisted by the steel brace system as shown in Fig. 2.

All girders, beams, columns, braces, and steel decks are made by hot-rolled H-section Q345 steel. The dimensions are listed in Table 1. As shown in Fig. 3, the thickness of the composite slab is 100 mm. The trapezoidal steel decks used in this test are 915 mm wide and 1.2 mm thick. The laying direction of the trapezoidal steel deck is parallel to the girder direction. The trapezoidal steel deck could be clasped along the transverse direction by the folding edges. The concrete slab is reinforced with 200 × 200 mm CRB550 welded steel fabric with a clear cover of 15 mm. The C30 concrete is used with the nominal compressive strength of 30 MPa. The steel beams and composite slab are connected with 16-mm-diameter, 80-mm-height shear studs. To achieve the composite action, a total of 13 shear studs are welded to each girder with 300-mm spacing, while 11 shear studs are welded to each beam with a spacing of 305 mm.

As indicated in Fig. 4, the welded flange-bolted web moment-resisting connection is adopted for girder-to-column connections. The complete-joint-penetration (CJP) groove weld is used to connect the girder flanges and shear tabs to the column flanges. Three M16 (16 mm in nominal diameter) Grade 10.9 frictional high-strength bolts are employed to connect the girder web with the extended shear tab. The beam-to-column and beam-to-girder connections are all connected with the extended single shear tab using two M16 Grade 10.9 frictional high-strength bolts. All high-strength bolts are applied with a pretightening force of 100 kN.

Test Specimen

The middle edge column at the first floor is assumed to be removed as shown in Fig. 1. The specimen, referred to as 2G1B-IN, is an exterior 2 × 1 bay substructure, as indicated by the dashed lines in Fig. 1. Its plan view and elevation view are shown in Fig. 5, where symbols of C, G, B, and P represent columns, girders, beams, and peripheral beams, respectively. The slab is extended by 900 mm to simulate the continuous boundary conditions provided by the neighboring spans. The extended slab is constrained by welding reinforcing bars and the steel deck to the peripheral beams, which have the same section size as that of the girders and are connected to the extended girders and beams as shown in Figs. 5 and 6. The trapezoidal steel deck is continuous without any overlapping in the direction parallel to the girder. The welded steel fabric has a lap splice of 600 mm above the B5 and B6 beams in order to keep the continuity of reinforcement. For the convenience of transportation, all the columns are divided into two parts, as shown in Fig. 5(b), one 600-mm stub and one 1,300-mm support column.

Simplification of Column

Because the floor is assumed to be restrained in plane, the lateral constraint contributed by the column could be neglected. The significantly lateral resistance provided by the surrounding frame system is verified by numerical simulation in the following section. Before the failure of the girder-to-column connection, the flexural capacity of the connection is a key source of the vertical resistance. The flexural capacity of the moment-resisting connection is highly affected by the joint rotational stiffness, therefore the column used in this test was designed to meet the original condition. Due to the limitation of the laboratory condition, the specimen cannot be fitted with full-height columns. As shown in Fig. 7, assuming the bottoms of the first-floor columns and the tops of the second-floor columns are fixed, the rotational stiffness of the two adjacent columns can be calculated by

$$k_{\text{adjacent}} = \frac{2 \times 4\text{EI}}{l} = \frac{8EI}{l} \tag{1}$$

At the same time, the rotational stiffness of a cantilever column with the same section but only a half-story height can be calculated by Eq. (2), which is equal to the rotational stiffness provided by the two adjacent columns. Therefore, the two adjacent columns can be replaced by a cantilever column with the length of half-story height (1.8 m).

$$k_{\text{cantilever}} = \frac{4EI}{0.51} = \frac{8\text{EI}}{l} = k_{\text{adjacent}} \tag{2}$$

Test Setup

The test setup is described in Fig. 8, where a load-distribution system is designed to uniformly distribute the point load from the 2,000-kN actuator to 24 loading points (Fig. 9) under a displacement-control loading scheme. As illustrated in Fig. 8, the load-distribution system has four levels, including seven strong beams and eight triangular steel plates. The strong beams except the third-level beam are connected by steel rollers and loosely restricted with bolts in an oblong slot, which forms a pin connection between different-level beams without losing stability. The third-level beam is connected to the fourth-level beam by a socket joint, which could allow possible rotation when the slab undergoes large deflection. The load of every fourth-level beam is distributed to three 300 × 300-mm square plates to avoid punching shear failure. In order to calculate the moment and shear force in the column

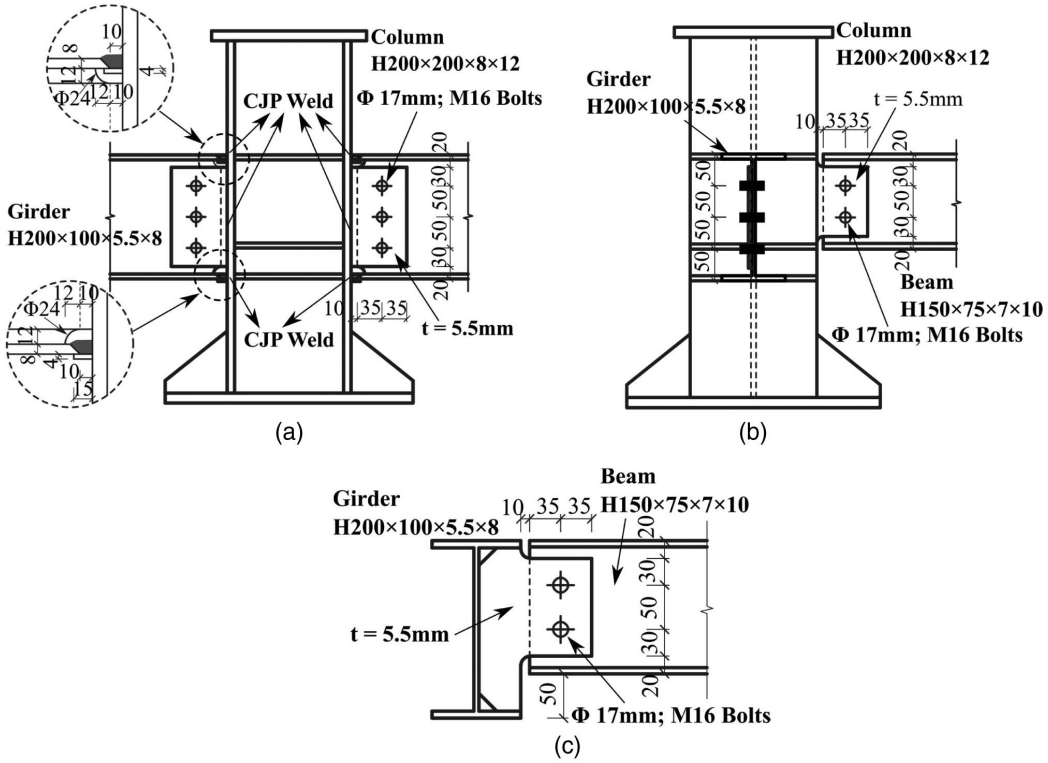

Fig. 4. Connection details of prototype structure (unit: millimeters): (a) welded flange—bolted web for girder-to-column connection; (b) extended shear tab for beam-to-column connection; and (c) extended shear tab for beam-to-girder connection.

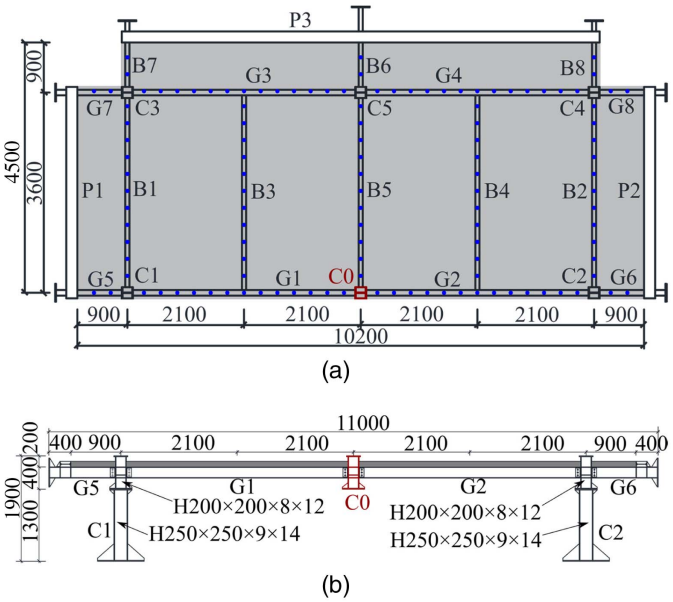

Fig. 5. Test specimen (unit: millimeters): (a) plan view; and (b) elevation view.

Fig. 6. Layout of 2G1B-IN before casting concrete.

through measured strains, it would be desirable to keep the strains within the elastic range. For this reason, as shown in Fig. 5(b), the support columns are replaced by the H250 × 250 × 9 × 14 (mm) hot-rolled steel. The change of the column section has limited influence on the overall behaviors of the floor system.

The horizontal movements of the extended girders, i.e., G5–G8, and the extended beams, i.e., B6–B8, are constrained by the horizontal supports to simulate the boundary condition provided by neighboring structural members. The horizontal supports connected to G5 and G6 are the most important in this test because the catenary force developed in G1 and G2 would be influenced by the stiffness of this horizontal support. The fully constrained assumption adopted for these horizontal supports is validated through a preliminary numerical analysis. As shown in Fig. 10(a), the prototype structure model is established in LS-DYNA R11, where the structural components representing the test specimen are removed. Beam elements with cross-section integration are used to model the column, girder, beam, and brace, while layered shell elements are adopted to represent the composite slab. The material properties in this model used the nominal yield values, i.e., 345 MPa for structural steel components and steel deck, 550 MPa for welded steel fabrics, and 30 MPa for concrete. An elasto-perfectly plastic stress-strain model is used to simulate the steel components, while a damage plastic model is used for the concrete. A pair of lateral forces are applied to the joints on behalf of the G5-C1 and G6-C2 connections in the test specimen, and the corresponding force-displacement curve of the G6-C2 joint is

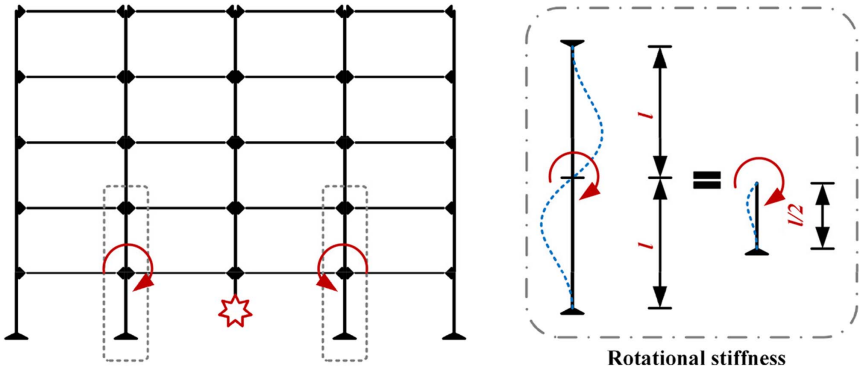

Fig. 7. Simplification of column.

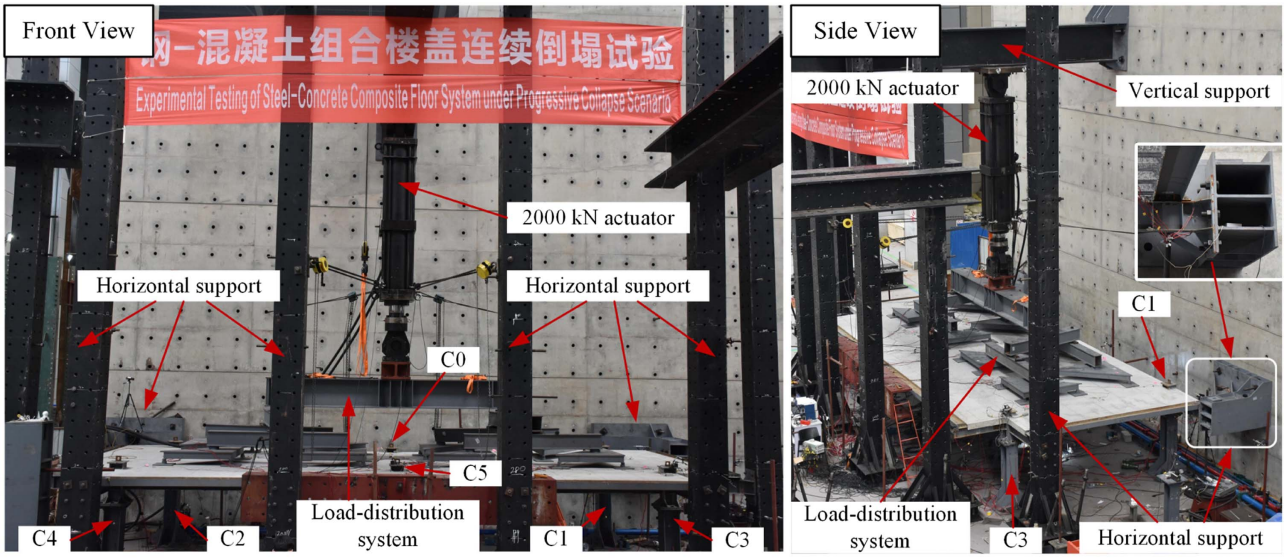

Fig. 8. Test setup and boundary conditions.

selected to be plotted in Fig. 10(b) along with the yield axial force (901 kN) of the G6 girder. The yield horizontal displacement of the structural model is 16 mm under a corresponding lateral force of 2,234 kN, and this horizontal displacement is merely 4 mm under an applied lateral force equal to the yield axial force of the G6 girder. Therefore, the fully constrained assumption for the horizontal supports connecting to G5 and G6 is reasonable.

Test Procedure

The middle edge column is cut into a stub 200 mm below the bottom flange of the girder section, leaving a 1,400-mm clearance above the ground. The midspan of the first-level distribution beam is subjected to a 2,000-kN actuator, which is vertically mounted onto a vertical resisting system and controlled with displacement loading. The loading rate of the actuator is 4 mm/min until the total failure of the specimen.

Instrumentation

The test specimen is monitored with a set of instruments to capture both global and local behaviors. A total of 36 linear variable differential transformers (LVDTs) are used in the specimen, where 21 LVDTs (marked by V) are used to capture the vertical deflection

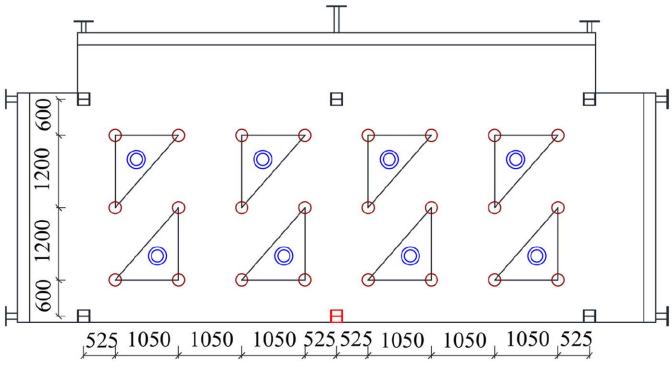

Fig. 9. Loading points of load-distribution system (unit: millimeters).

patterns of the floor system and 15 LVDTs (marked by H) are used to measure the possible horizontal movement in the peripheral members. Uniaxial strain gauges are used to measure strains from columns, girders, beams, trapezoidal steel decks, and welded steel fabrics. The measured strains are used to analyze the stress and load redistribution of the specimen. In the following sections,

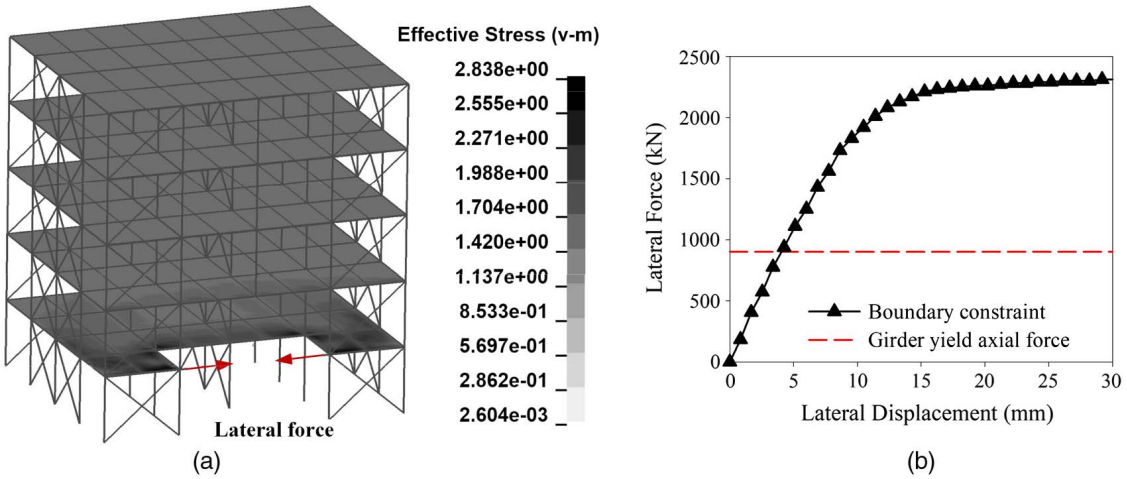

Fig. 10. Lateral constraint of the test specimen: (a) prototype structural model; and (b) force-displacement curve of lateral constraint.

Table 2. Summary of material properties measured from coupon tests (dimensions in millimeters)

Components	Location	Initial thickness	f_y (MPa)	f_u (MPa)	Reference length	Rupture length	Elongation[a]
Girder/peripheral	Flange	7.7	390	536	80	105	0.31
beam	Web	5.3	419	557	70	92	0.31
Beam	Flange	9.3	365	517	90	118	0.31
	Web	6.5	400	535	75	99	0.32
Column H200 × 200	Flange	11.6	373	531	100	132	0.32
	Web	7.8	395	546	80	105	0.31
Column H250 × 250	Flange	13.4	383	536	110	142	0.29
	Web	8.6	405	551	85	107	0.26
Steel deck	Slab	1.18	320	380	60	83	0.38
Rebar	Slab	Φ 8	596	672	50	53.3	0.07
Shear stud	Slab	Φ 16	320	400	—	—	0.14
Bolt	Connection	Φ 16	940	1,040	—	—	0.10

[a]Elongation = (Rupture length) / (reference length) − 1.

the vertical displacement of the removed column is represented by δ, which is calculated by the average value of the measured displacements from two LVDTs attached to the bottom end of the removed column.

Material Properties

The steel properties of the columns, girders, beams, and trapezoidal steel decks are listed in Table 2 as well as the material property of the welded steel fabrics. Coupon tests were carried out to obtain these steel properties. The values of elongation are calculated based on the reference length and the rupture length. No coupon test has been conducted for the shear studs and high-strength bolts. Therefore, the nominal material properties provided by the manufacturers are listed in Table 2.

The concrete is C30 grade cast-in-place concrete with an average compressive strength of 32.83 MPa from 150 × 150 × 150-mm cubes. Two shear stud push-out tests were conducted to investigate the composite behavior and to provide test data for the numerical model validation in the future study. As shown in Fig. 11, Specimen 1 is designed to represent the shear stud connection along the girder direction and Specimen 2 represents the connection along the beam direction. The materials used in the push-out specimens are identical to those of Specimen 2G1B-IN. Displacements are measured by the built-in transducer of the actuator. The relative load-displacement curves are plotted in Fig. 12, showing a better performance of Specimen 1 compared to Specimen 2 in terms of capacity (about two times higher) and ductility.

Response of the Specimen

Failure Process

The load-displacement curve is plotted in Fig. 13. The load F is measured from the actuator, while the vertical displacement δ is calculated by the average value of the measured displacements from two LVDTs attached to the C0 column. The uniformly distributed load ω is approximately calculated by dividing load F by the area of the 2 × 1 bay slab (8.4 × 3.6 m = 30.24 m^2). The chord rotation angle of girder θ is calculated by dividing δ by the girder span (4.2 m). Considering the self-weight of the specimen (66.4 kN) and the weight of the load-distribution system (44 kN), there is an equivalent initial distributed load of 3.65 kN/m^2 before loading. The failure process of Specimen 2G1B-IN will be described according to the load-displacement curve as follows.

When the vertical displacement reached 70 mm (0.0167 rad, Point A), cracks were observed at the slab top surface along the C1-C3-C5-C4-C2 lines due to the sizeable negative moment.

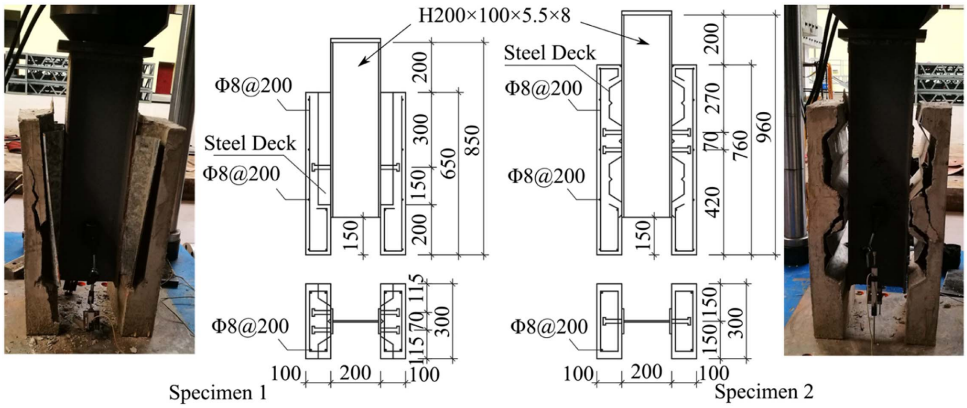

Fig. 11. Push-out specimens (unit: millimeters).

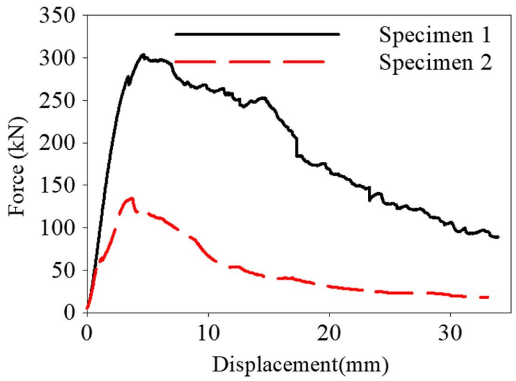

Fig. 12. Load-displacement curves of push-out specimens.

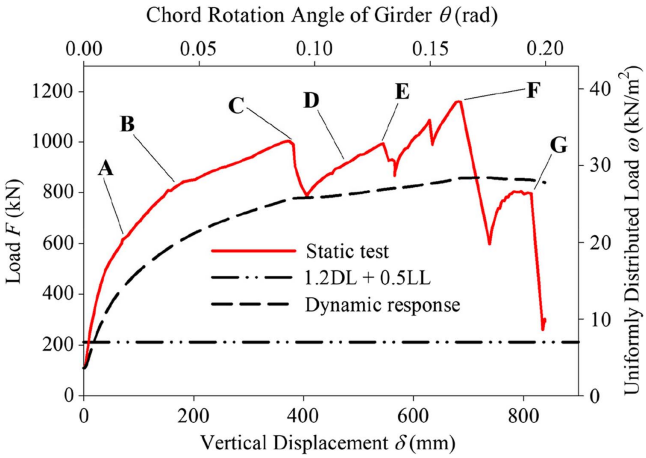

Fig. 13. Load-displacement curve of 2G1B-IN.

As the vertical displacement reached 170 mm (0.04 rad, Point B), cracks were observed at the slab area right above the B3-G1 connection and the B4-G2 connection because of the excessive shear forces transferring from the B3 and B4 beams [Fig. 14(a)]. Local buckling was also observed at the bottom girder flanges of the G1-C1 connection and the G2-C2 connection due to the negative moment at these locations. When the vertical displacement further increased to 380 mm (0.09 rad, Point C), the applied load suddenly dropped from 1,000 to 770 kN because of the abrupt fracture of the top girder flange at the G1-C1 connection [Fig. 14(b)]. In the meantime, the tensile force once carried by the top flange transferred to the nearby steel deck, leading to the development of tiny cracks in the steel deck. The G1 and G2 girders and the slab above them slightly twisted as a result of the excessive vertical loads imposed on the nearby slab [Fig. 14(c)]. Severe horizontal cracks developed at the midslab surface area above the B3-G1 connection and the B4-G2 connection, because the concrete above the shear stud slipped under the compression parallel to the girder axis. At the same time, the slab cracks at the negative moment locations became wider and deeper. As the vertical displacement reached 480 mm (0.114 rad, Point D), the bottom bolts at the B5-C5 connection sheared off [Fig. 14(d)]. In addition, the horizontal cracks at the midslab surface area above the B3-G1 connection and B4-G2 connection developed rapidly. As the displacement continuously increased to 550 mm (0.131 rad, Point E), the fracture of the top girder flange at the G2-C2 connection [Fig. 14(e)] led to a sudden decrease of load from 995 to 870 kN, indicating the diminishing of the flexural-resisting mechanism of the composite girders as the G1-C1 connection and G2-C2 connection both failed at this point. As shown in Fig. 14(f), the slab adjacent to the C2 column suffered the punching shear failure. Due to the serious twist of the G1 and G2 girders and neighboring slab [Fig. 14(c)], the slabs near the G1-C1 and G2-C2 connections were separated from the girders with the shear studs exposed. After that, the connections between the steel deck and the P1 and P2 beams also started to fail, and the steel deck moved inward under the membrane force, causing the excessive twist of the B1 beam.

The floor system achieved its maximum resistance of 1,159 kN as the displacement reached 686 mm (0.163 rad, Point F), followed by the complete rupture of the girder section at the G1-C1 connection [Fig. 14(g)]. The load suddenly dropped to 560 kN, indicating the loss of the load-resisting mechanism provided by the catenary action. The slab adjacent to the C1 and C2 columns was torn apart, and the shear studs were directly exposed. The shear studs near the G1-C1 connection and the B3-G1 connection were sheared off as shown in Fig. 14(h). After the rupture of the G1 girder, the released load was redistributed to the nearby B1-C1 connection. The failure of the connection between the welded steel fabrics and the P1 beam was also observed.

With the further increase of the vertical displacement, the load resistance gradually stabilized at 790 kN, which was considered to be mostly provided by the tensile membrane action. At the vertical displacement of 815 mm (0.194 rad, Point G), the shear tab at the B1-C1 connection fractured. Meanwhile, the total cross section of the neighboring trapezoidal steel deck (915 mm wide) fractured

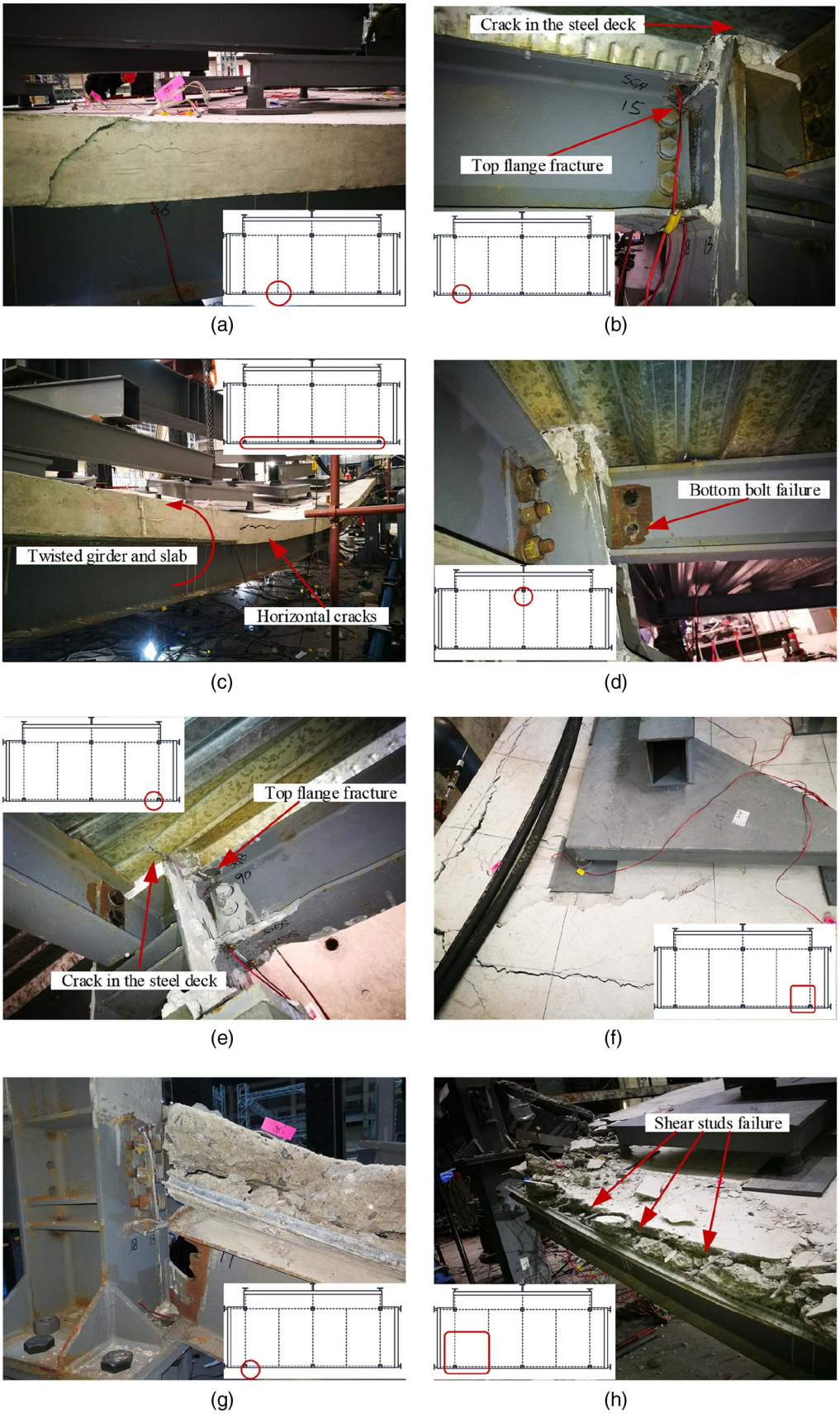

Fig. 14. Failure phenomenon in the loading process: (a) slab cracks above the B3-G1 connection; (b) top flange fracture at the G1-C1 connection; (c) slab damages above the G1 and G2 girders; (d) bottom bolt cut off at the B5-C5 connection; (e) top flange fracture at the G1-C1 connection; (f) punching shear failure near C2 column; (g) failure of the G1-C1 connection; and (h) slab damages near C1 column at the displacement of 815 mm.

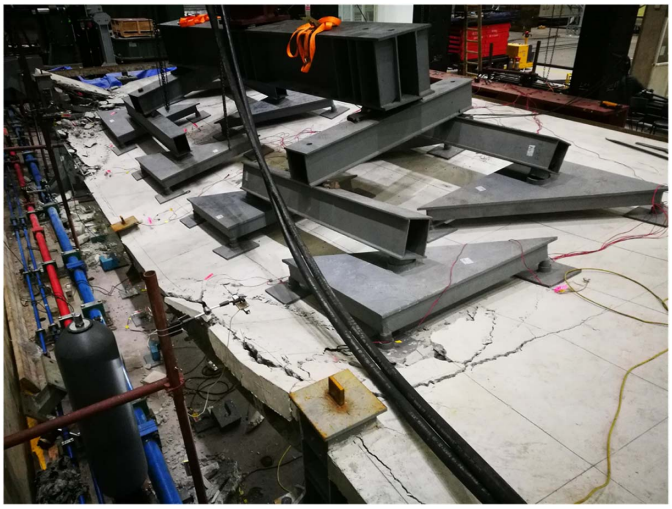

Fig. 15. Failure phenomenon at the end of the test.

along the B1 beam direction. Above the fractured section of the steel deck, a total of four bars of the weld fabrics ruptured. The test was terminated as the floor system lost its load-carrying capacity. However, there was no apparent difference in terms of damage near the removed column, comparing between the final stage and the loading stage at the vertical displacement of 70 mm (Fig. 15).

Strain Measurements

Trapezoidal Steel Deck

Considering the symmetry of the specimen, the locations of strain gauges at the trapezoidal steel decks and the measured results are plotted in Fig. 16, where the dot-dashed lines represent the yield strain of the steel deck. As shown in Fig. 16, unlike the innermost SD3, the measured strains at SD1 and SD2 were tensile during the entire loading process. SD1 and SD2 reached the yield strain at the vertical displacement of 600 mm, while SD4 and SD5 reached the yield strain earlier at a vertical displacement of about 380 mm. It implied that the tensile membrane action was first developed in the outer region of the slab. When the vertical displacement exceeded 650 mm, the strain at SD4 started to decrease due to the propagation of the crack in the steel deck near the C1 column. The strain at SD3 was compressive initially, then gradually became tensile as the vertical displacement increased. The measured strains at SD3 and SD6 did not reach the yield strain during the test.

Welded Steel Fabric

Due to the symmetry of the specimen, the locations of the strain gauges attached to the welded steel fabrics and the measured results are plotted in Fig. 17, where the dot-dashed lines indicate the yield strain of the welded steel fabrics. As shown in Fig. 17(a), SR1 developed a tensile strain much earlier than SR3, where the tensile strain was seen after the vertical displacement exceeded 400 mm. SR2 failed in the early stage due to a slab crack right through it. For SR6, SR7, and SR8, the tensile strains were observed until the vertical displacement was beyond 400 mm, and SR6 developed the highest tensile strain, while SR8 developed the least, indicating more tensile forces in the slab were developed in the outer regions. For SR11, SR12, and SR13, a similar phenomenon could also be observed, with SR11 developing the highest tensile strain while the strain at SR13 was compressive. Along the beam direction, SR16, SR17, and SR18 were in tension during the loading process. This was because the slab along the beam direction behaved as a cantilever beam when deflecting under loads. As shown in Fig. 17(b), the increasing trend of the tensile strain at SR16 stopped when the vertical displacement reached 580 mm. After that, the tensile strain started to decrease rapidly, which was caused by the damage of concrete above the B3-G1 connection.

Girder Flanges

The measured strains of the G1 and G2 girder flanges are shown in Fig. 18. The top girder flanges at both sides of the removed column were in tension from the initial loading state, indicating that the neutral axis of the composite sections was located in the slab. The measured strains from the top and bottom flanges at the midspan show a typical flexural behavior of the girder section, caused by the excessive shear force from B3 and B4 beams. At the composite section adjacent to the G1-C1 connection, the top flange was in tension and the bottom flange was in compression, which implied that the neutral axis was located in the steel girder section. It is worth mentioning that the location of the neutral axis in this test is different from that in the test conducted by Johnson et al. (2015), where a similar specimen with simple shear connections was tested. In their study, the neutral axis of the composite sections near the removed column was located in the composite slab, but the neutral axis of the composite sections near the adjacent columns was also located in the slab. Furthermore, the neutral axis was located at the center of the beam section in the bare steel moment frame specimen tested by Li et al. (2017).

Compared to the tests conducted by Johnson et al. (2015) and Li et al. (2017), the moment connection and the composite slab greatly enhance the moment-resisting capacity of the girder-to-column

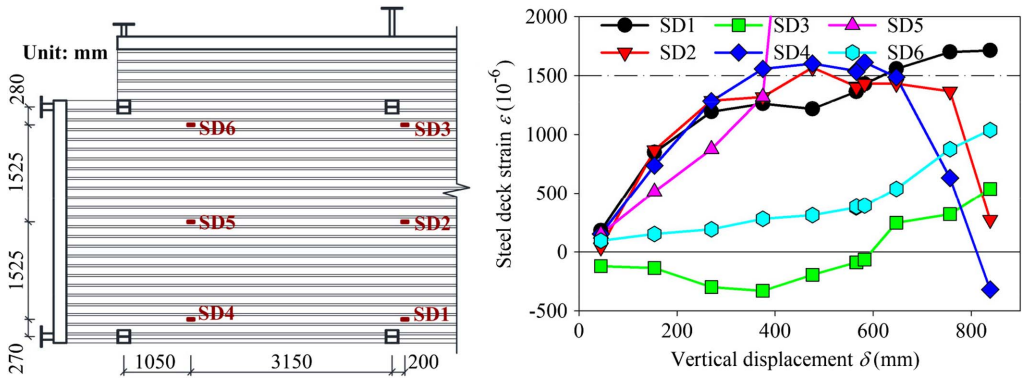

Fig. 16. Strains measured from the steel deck.

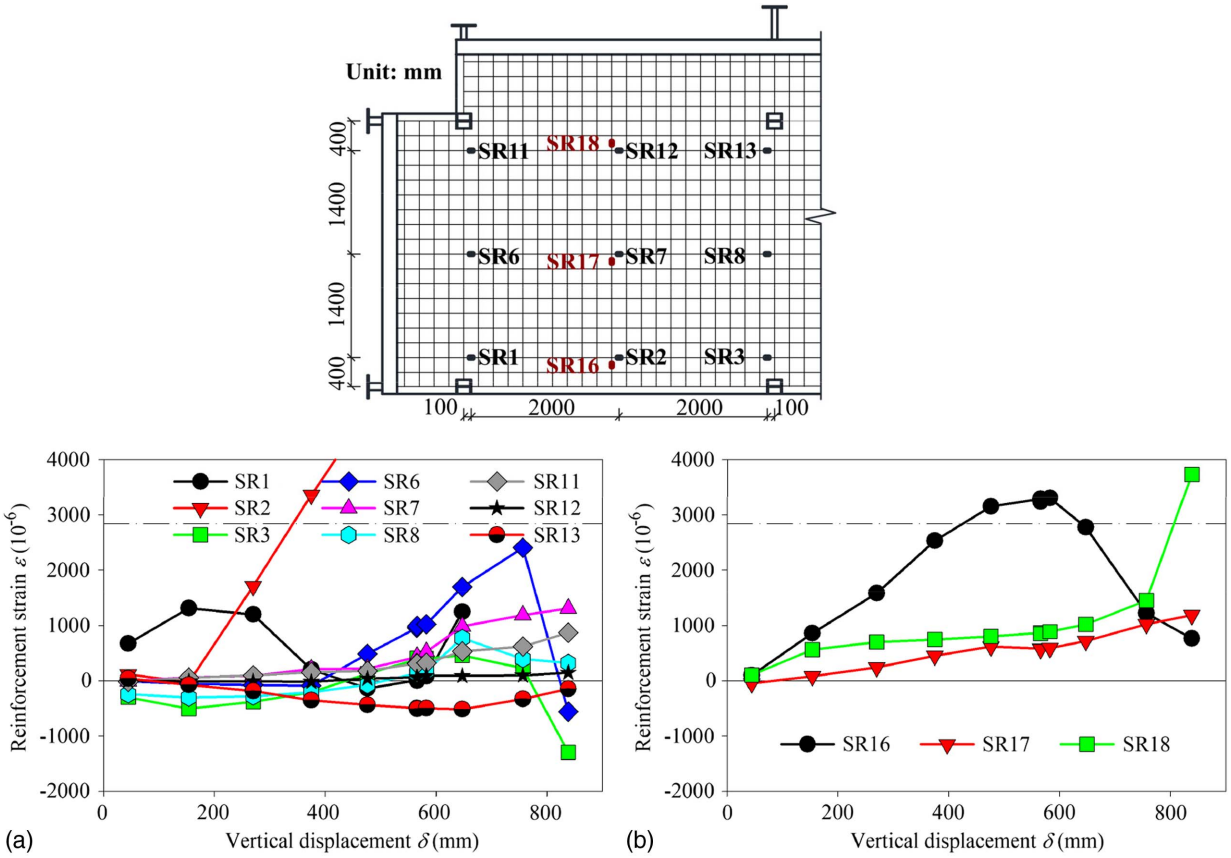

Fig. 17. Strains measured from the welded steel fabric.

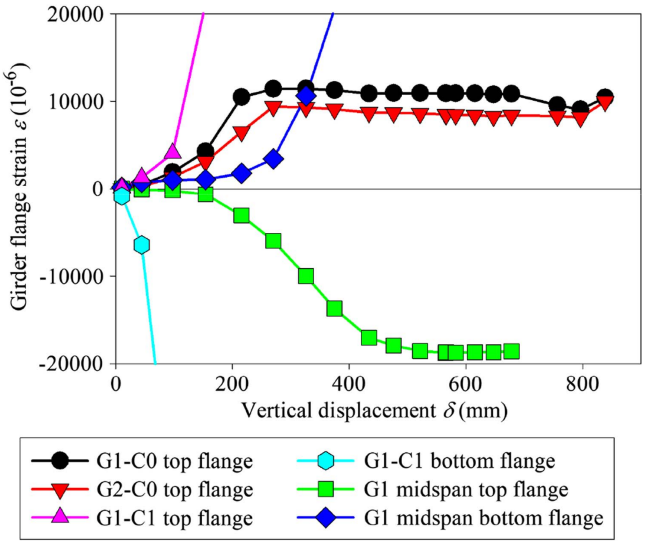

Fig. 18. Strains measured from the girder flanges of G1 and G2.

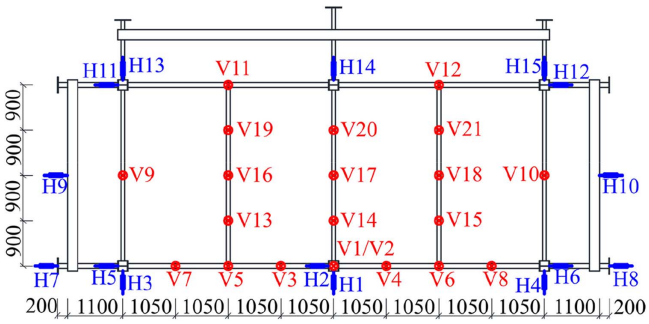

Fig. 19. Locations of the LVDTs (unit: millimeters).

connections. For the girder-to-column connection near the adjacent columns (C1, C2), the composite slab could not generate too much tension under the negative moment, but the moment connections could resist a much higher negative moment than the simple shear connection. For the girder-to-column connection near the removed column, the girder and composite slab could work together and resist a much higher positive moment than the bare steel connections.

Vertical Deflection and Horizontal Displacement

The locations of the LVDTs are shown in Fig. 19. The contour of the slab vertical deflection at the vertical displacement of 650 mm is plotted in Fig. 20. With the increase of the vertical displacement, the deflection shape of the floor system is mostly symmetric about the B5 beam until the complete rupture of the G1-C1 connection. The vertical displacements at the midspan of B1 and B2 beams are plotted in Fig. 21.

The horizontal movements of the specimen boundary are described in Fig. 22. The movements toward the center of the specimen are defined as positive, and movements away from the center are defined as negative. The horizontal displacements along the girder direction at the C1 and C2 columns (H5 and H6, respectively) were almost identical before the vertical displacement reached 500 mm. After that, the horizontal displacement at the

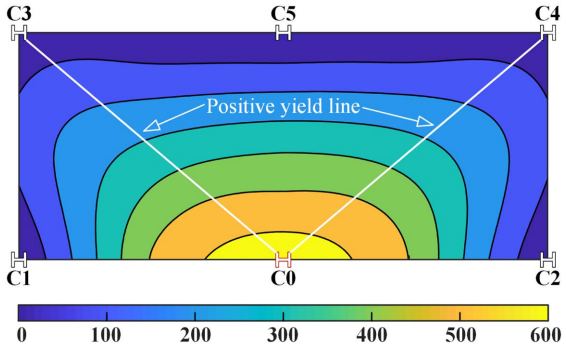

Fig. 20. Vertical deflection of the floor system at the displacement of 650 mm (unit: millimeters).

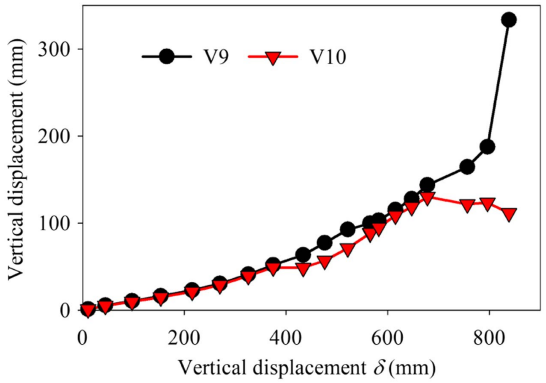

Fig. 21. Vertical displacement at the midspan of B1 and B2 beams.

C2 column (H6) exceeded the displacement at the C1 column (H5) due to the developing damage of the G1-C1 connection after the fracture of the top girder flange. As reflected by H7 and H8, notable horizontal movements at the horizontal supports connected to G5 and G6 were developed during the test. Such movements were induced by the gap between the anchor bolt and the anchor hole. Its influence on the development of horizontal boundary forces will be discussed later. As shown in Fig. 22(b), the horizontal movements perpendicular to the girder direction at the C1 and C2 columns (H3 and H4, respectively) were outward when the vertical displacement was less than 500 mm, which implied that the compressive arch action was developed in the B1 and B2 beams. As the vertical displacement increased to 560 mm, the movements of H3 and H4 were turned inward due to the deflection increasing of the B1 and B2 beams (Fig. 21). As shown in Fig. 22(b), the horizontal movements parallel to the girder direction at the C3 and C4 columns (H11 and H12, respectively) were not significant in this test, which implied that the horizontal forces at these locations were not as significant as those in the C1 and C2 columns. The horizontal movements at the midspan of the P1 and P2 beams (H9 and H10, respectively) were inward because P1 and P2 were pulled inward by the tensile forces transferred from the steel deck and weld fabrics. Because the damage at the connection of the slab and P2 was more severe than that related to P1, the inward movement at the P2 midspan (H10) was higher. Based on the previous observations, the movement tendency near the C1 and C2 columns is illustrated in Fig. 22(c).

Slab Crack Pattern

The crack pattern of the slab top surface at the end of the test is shown in Fig. 23(a). After the failure of the G1-C1 and G2-C2 connections, the tensile forces previously carried by the girder-to-column connections were redistributed to the neighboring slab, which caused the severe concrete spalling near the C1 and C2 columns. Meanwhile, concrete crushing was not observed at the slab surface near the removed column C0 as the result of the relatively minor damage at the G1-C0 and G2-C0 connections. The cracks developed in the surrounding negative moment areas indicate the formation of negative yield lines in this area. These negative yield lines are represented by the dashed lines in Fig. 23(a). According to the test conducted by Sawczuk and Jaeger (1963), Qian and Li (2015), Qian et al. (2016), and Lu et al. (2017), the positive yield lines can be reflected by the crack pattern on the bottom surface of the slab. Because the bottom surface of the slab is covered by the steel deck in this test, the crack patterns obtained through numerical simulation are used to determine the positive yield lines. The corresponding numerical simulation is conducted by Wang et al. (2019), and the concrete cracks on the bottom surface of the slab are shown in Fig. 23(b). As shown in Fig. 23(b), diagonal concrete cracks are developed along the C0-C3 and C0-C4 directions, which implies that positive yield lines are formed in these directions. Moreover, the positive yield lines can also be indirectly reflected by the gradient field of the slab vertical displacement in Fig. 20. The contour lines significantly change direction near the C3-C0 and C4-C0 diagonal lines, which indicates positive yield lines forming along these diagonal lines. Besides, as shown in Fig. 23, compressive rings are observed at the outer region of the slab, and the compressive forces developed in this region can partially balance the tensile forces developed near the removed column. A similar crack pattern was also observed in the tests conducted by Lu et al. (2017) and Lim et al. (2017). It is worth noting that there were several horizontal cracks formed at the midslab surface which were parallel to the girder axis. These horizontal cracks were caused by the tension force developed along the beam axis direction, which could be reflected by the measured strain of the welded steel fabric in Fig. 17(b). Besides, these horizontal cracks also imply that the tensile membrane action was partially developed along the beam axis direction.

Discussion of the Test Results

Horizontal Force at the Boundary

As shown in Fig. 24, the cross sections at heights of H_1 (1,000 mm) and H_2 (500 mm) of the support column were assigned sufficient strain gauges to calculate the moments at these sections, i.e., M_1 and M_2. Because all the measured column sections remain elastic and keep deforming as plane sections, M_1 and M_2 are calculated according to Eq. (3). $\Delta\varepsilon/\Delta h$ represents the curvature of the column, while $\Delta\varepsilon$ and Δh represent the difference between the measured strains of two strain gauges and their responding distance, respectively. The shear force V in the column could be statically determined through Eq. (4). The axial force F_{boundary} in the extended girder or beam could be derived by the measured strains at the girder or beam section. The horizontal force F_{tension}, representing the resultant of all horizontal forces at the girder-column connection or beam–column connection, could be obtained by Eq. (5)

$$M = EI\frac{\Delta\varepsilon}{\Delta h} \tag{3}$$

$$V = \frac{M_2\text{-}M_1}{H_1\text{-}H_2} \tag{4}$$

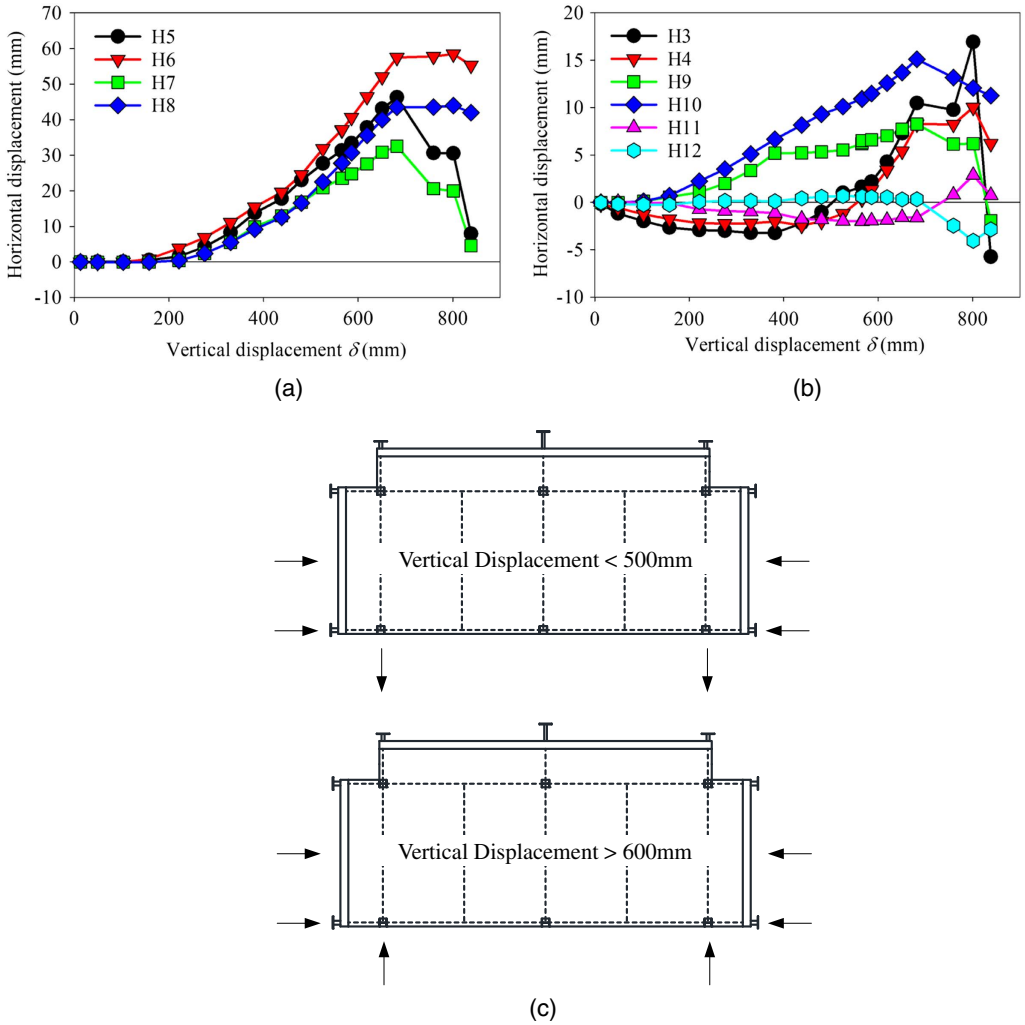

Fig. 22. Horizontal displacement of boundaries (inward movement is positive, outward movement is negative).

$$F_{tension} = F_{boundary} + V \quad (5)$$

$F_{tension}$ at each boundary column is plotted in Fig. 25. As shown in Fig. 25(a), the values of the horizontal forces paralleled to the girder direction at the C1 and C2 columns were negative before the vertical displacement reached 210 mm, indicating that compressive forces had developed due to the compressive arch action. Along the girder direction, the horizontal forces at the C3 and C4 columns were relatively small and insignificant. Along the beam direction, as shown in Fig. 25(b), initially a higher compressive force at the C5 column was observed compared to the forces at the C3 and C4 columns. When the vertical displacement exceeded 680 mm, the horizontal force at the C3 column turned into tension while the compressive force at the C4 column increased and exceeded the horizontal force at the C5 column. This was because the failure at the G1-C1 connection destroyed the symmetry of the structure. After the failure of the G1-C1 connection, the vertical displacement of the neighboring slab suddenly increased, which caused the load-distribution system to rotate slightly around the actuator. Becuase of this rotation, the load-distribution system was moved closer to the C4 column and away from the C3 column, which resulted in the changes in the horizontal forces at the C3 and C4 columns.

As shown in Fig. 22(a), the horizontal supports connected to G5 and G6 were moved during the test, which was caused by the gap between the anchor bolt and the anchor hole. In the test, the diameter of the anchor bolts was 36 mm, while the diameter of bolt holes on the reaction wall and horizontal supports was 60 mm. Because the two horizontal supports behaved similarly, only the lateral force versus the lateral displacement curve of the horizontal support connected to G5 is plotted in Fig. 26. As implied by the force-displacement curve, before the lateral displacement reached 23 mm, the lateral force was mainly supplied by the friction between the support and the reaction wall. When the lateral displacement exceeded 23 mm, the lateral force increased rapidly as a result of the bearing force between the anchor bolt and the bolt hole.

Load-Resisting Mechanism

As shown in Fig. 13, the vertical load reached its first peak of 1,000 kN at the flexural stage when the vertical displacement increased to 380 mm. After that, the fracture of the top girder flange at the G1-C1 connection led to a sudden drop of the applied load, which marked the transition from the flexural stage to the catenary-membrane stage. As the vertical displacement increased to 686 mm, the vertical load reached its maximum of 1,159 kN, followed by the complete rupture of the section of the G1 girder. Before the failure of the G1 girder, the vertical resistance was mainly provided through the catenary action and the tensile membrane action. After the failure of the G1 girder, the catenary action diminished, and the tensile membrane action mainly contributed to

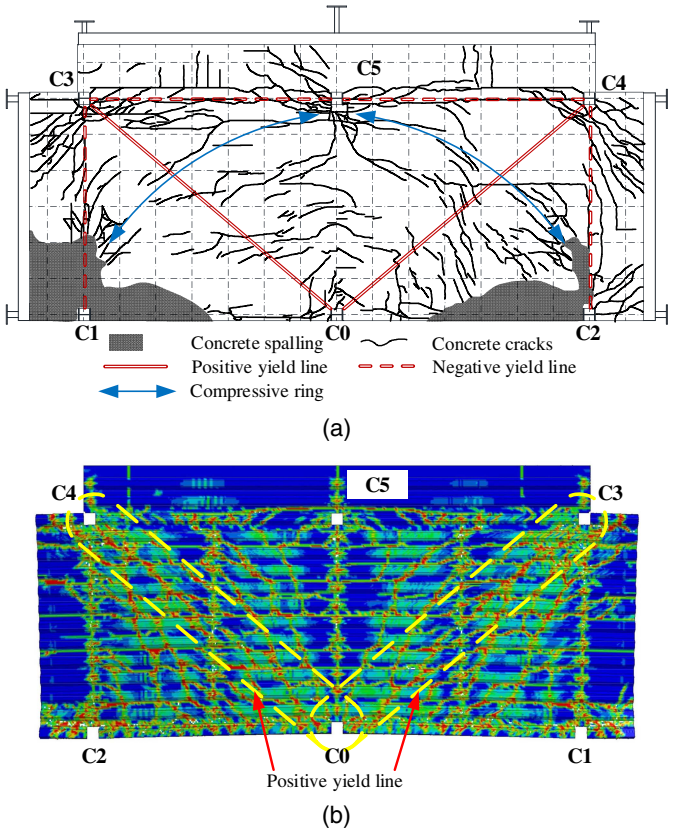

Fig. 23. Crack patterns on the concrete slab: (a) slab top surface; and (b) slab bottom surface.

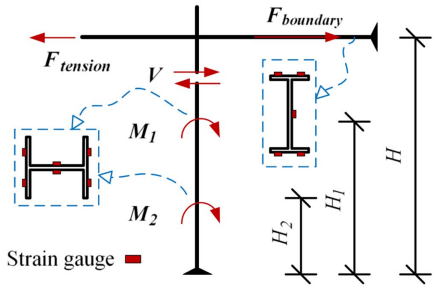

Fig. 24. Horizontal forces at the boundary columns.

the vertical resistance. Comparing the peak loads at the flexural stage and the catenary-membrane stage, the combined resistance from the catenary action and the tensile membrane action was 15.9% higher than that from the flexural action alone. Similarly, in the numerical simulation by Alashker et al. (2010) and experimental test by Fu et al. (2017), the resistance improvement ratios between the flexural action contribution and the combined contribution of the catenary action and the tensile membrane action were also not more significant than the resistance improvement ratio from the bare steel frame test conducted by Li et al. (2017). In other words, the load-displacement curve of the bare steel frame test was steeper than that of the frame including the composite slab. This indicated that the composite slab not only provided tensile membrane action but also notably enhanced the flexural resistance through the beam-slab composite action.

In the flexural stage, compressive arch action had been generated along both the girder direction and the beam direction. As shown in Fig. 25(a), before the vertical displacement reached 210 mm, the horizontal compressive forces at the C1 and C2 columns indicated the development of the compressive arch action along the girder direction. Along the beam direction, the compressive arch action was reflected by the horizontal outward movements at the C1 and C2 columns. According to the research of Park and Gamble (2000) and Su et al. (2009), the maximum compressive arch action would be generated before the deflection reached the half-depth of the concrete section, and this arch action could lead to an outward movement at the horizontal boundary. When the deflection exceeded the depth of the concrete section, the arch action and the outward movement would be diminished. The depth of the concrete slab section without the plate-rib is 50 mm. As shown in Fig. 21, when the vertical deflections at the midspan of the B1 and B2 beams reached half the depth of the concrete section, i.e., 25 mm, the corresponding vertical displacement δ was about 230 mm. At the same time, the outward movements of H3 and H4 [Fig. 22(b)] almost reached their peak values, which implied that the compressive arch action in the B1 and B2 beams also reached its peak. When the vertical displacement δ increased to 400 mm, the deflections at the midspan of the B1 and B2 beams were about 50 mm, i.e., the depth of the concrete section. Meanwhile, the outward movements of H3 and H4 also began to diminish, which implied the decrease of the compressive arch action in the B1 and B2 beams.

Flexural Stage

Fig. 23 shows that several yield lines are explicitly formed in the concrete slab. Therefore, the yield-line theory is used to predict the load carried by the flexural mechanism. As shown in Fig. 27,

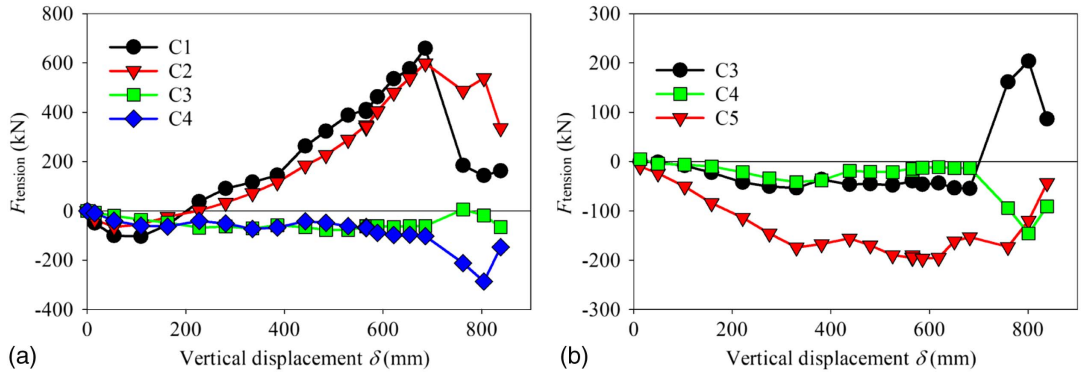

Fig. 25. Development of the horizontal force at each boundary column: (a) along girder direction; and (b) along beam direction.

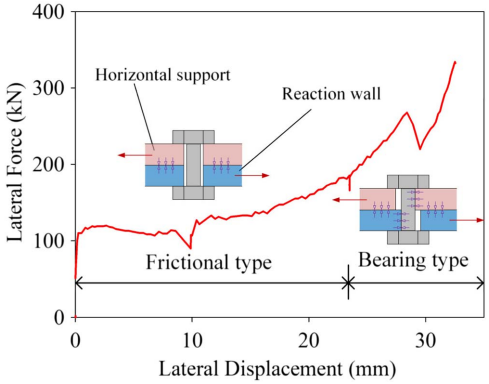

Fig. 26. Lateral force–lateral displacement curve of the horizontal support connected to G5.

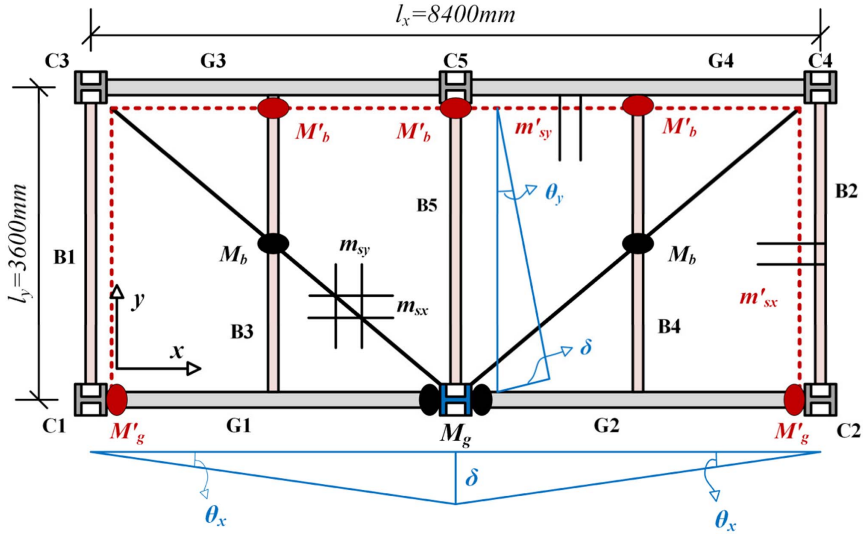

Fig. 27. Yield-line configuration of the test specimen.

the yield-line configurations of the specimen, l_x (8,400 mm) and l_y (3,600 mm), are the total lengths of the slab in the x- and y-directions, respectively, and θ_x (equal to $2\delta/l_x$) and θ_y (equal to δ/l_y) are the rotations about the y- and x-axis, respectively. δ is the vertical displacement at the C0 column, M_g and M'_g are the ultimate positive and negative bending moments of the girders, and M_b and M'_b are the ultimate positive and negative bending moments of the beams. The contribution of the composite slab to the bending moments of girder and beam has been considered. m_{sx} and m_{sy} are the ultimate positive bending moments of the per-unit width composite slab in the x- and y-directions, respectively, and m'_{sx} and m'_{sy} are the ultimate negative bending moments of the per-unit width composite slab in the x- and y-directions, respectively. All the ultimate bending moments are calculated according to Johnson (2004), and the results are listed in Table 3.

The internal virtual work W_{internal} produced by the positive and negative bending moments on the beam plastic hinges and the slab yield lines is calculated by

$$W_{\text{internal}} = (2m'_{sx}l_y + 2m_{sx}l_y + 2M_g + 2M'_g)\theta_x + (m'_{sy}l_x + m_{sy}l_x + 2M_b + 3M'_b)\theta_y \quad (6)$$

The external virtual work W_{external} done by the downward uniform distributed load ω on the slab is

Table 3. Ultimate bending moments of beams and slabs

Components	Bending moment (kN · m)
M_g	178.0
M'_g	78.1
M_b	124.5
M'_b	17.9
m_{sx}	31.3
m'_{sx}	11.3
m_{sy}	3.7
m'_{sy}	3.1

$$W_{\text{external}} = \omega l_x l_y \delta/3 \quad (7)$$

ω can be derived by $W_{\text{internal}} = W_{\text{external}}$ as

$$\omega = \frac{3}{l_x l_y}\left[\frac{2(2m'_{sx}l_y + 2m_{sx}l_y + 2M_g + 2M'_g)}{l_x} + \frac{(m'_{sy}l_x + m_{sy}l_x + 2M_b + 3M'_b)}{l_y}\right] \quad (8)$$

Based on the bending moment in Table 3, the yield-line prediction of the maximum distributed load ω is 29.3 kN/m^2, e.g., the

equivalent force F (equal to $\omega l_x l_y$) of 886.0 kN. The measured maximum vertical resistance of the specimen is 1,000 kN (at $\delta = 380$ mm), which is a little higher (12.9%) than the yield-line prediction. Steel strain hardening may contribute to the higher measured resistance. The reasonable prediction by the yield-line theory implies that the load-carrying capacity in this stage is mainly provided by the flexural mechanism.

Catenary-Membrane Stage

The resisting force from catenary action could also be calculated by the tensile forces in the girders, as illustrated in Fig. 28. At the displacement of 686 mm, the sudden drop of the load was caused by the fracture of the web and bottom flange of the G1 girder. Hence, the tensile force F_G in G1 could be calculated by Eq. (9), i.e., the yield tensile force provided by the web and bottom flange of G1. In Eq. (9), $f_{y,\text{web}}$, $f_{y,\text{flange}}$, A_{web}, and $A_{\text{bottom flange}}$ represented the yield stress of the girder web, the yield stress of the girder flange, the cross-sectional area of the girder web, and the cross-sectional area of the girder bottom flange, respectively. The resistant load (F_{C0}) from the catenary action generated in the G1 and G2 girders could be obtained by Eq. (10) as 222.4 kN. The rest of the resistant force (936.6 kN) was contributed by the composite slab. Therefore, the contribution percentages of the steel girder and the composite slab are 19.2% and 80.8%, respectively

$$F_G = f_{y,\text{web}} A_{\text{web}} + f_{y,\text{flange}} A_{\text{bottom flange}} = (419 \times 160 \times 5.5 + 390 \times 100 \times 8)N = 680.7 \text{ kN} \quad (9)$$

$$F_{C0} = \frac{2F_G \delta}{l_G} \quad (10)$$

As illustrated in Fig. 29, only the one-way tensile membrane action parallel to the free edge is sufficiently activated for the middle-edge-column removal scenario (Mitchell and Cook 1984). It is different from the fully restrained interior panels, which could take advantage of the two-way tensile membrane action. In this sense, the membrane action would play a more significant role in the internal-column removal scenario.

After the complete rupture of the girder section, the catenary action was diminished and the vertical resistance mainly relied on the composite slab. The vertical load at this stage did not surpass the peak load from the combined tensile membrane and catenary action. Nevertheless, the membrane action lasted longer in the floor system than the catenary action. Considering that the effectiveness of the catenary action is sensitive to the damage of the girder-to-column connections, the tensile membrane action is a relatively reliable resisting mechanism compared to the catenary action. As suggested by Sadek et al. (2008), measures that could potentially improve the membrane action, such as increasing the thickness of the steel deck, increasing the slab reinforcement ratio, and applying more shear stud to the girders and beams, are desirable to enhance the collapse resistance of the composite floor system.

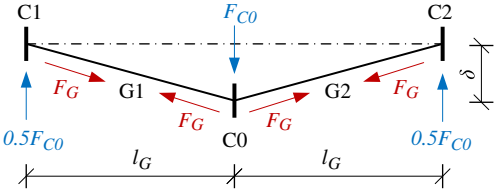

Fig. 28. Catenary action.

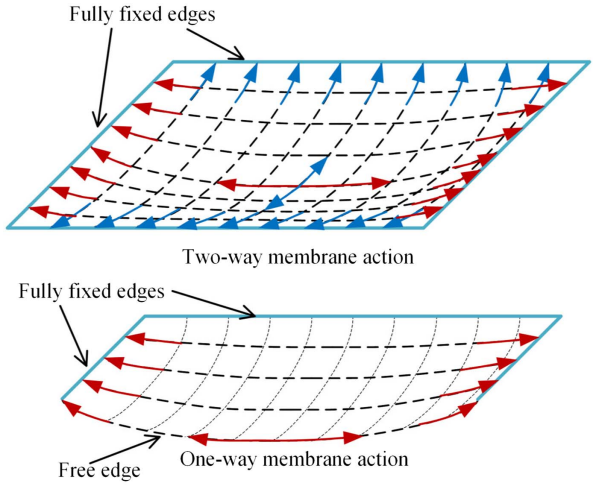

Fig. 29. Effects of boundary condition on the membrane action.

According to the ASCE/SEI 7-16 (ASCE 2017), a line representing the load combination for extraordinary events is drawn in Fig. 13. The load-resistant capacity of the test specimen at the flexural stage and the catenary-membrane stages are 4.7 times and 5.5 times that of the ASCE load combination, respectively, far greater than the load increase factor of 2.0 in DoD (2016). Based on the energy method proposed by Izzuddin et al. (2008), the approximate dynamic response is also generated and illustrated in Fig. 13. The peak dynamic resisting capacity is 4.1 times that of the ASCE load combination for extraordinary events, implying that the composite floor system designed according to the current design specifications can withstand the sudden removal of the middle edge column. Furthermore, compared with the test results from Johnson et al. (2015) and Hadjioannou et al. (2018), where the discontinuous steel deck and simple shear connections were used in their specimens, the continuous steel deck and moment-resisting connections adopted in this test significantly improved the loading-carrying capacity and the deformation capacity of the floor system.

Load Redistribution of the Column

When a column is suddenly removed, the load resisted by the removed column will be redistributed to neighboring columns. The load redistribution ratio can reflect the alternative load path formed during the load redistribution. In this study, the load redistribution ratio of each column is computed by dividing the axial force in each

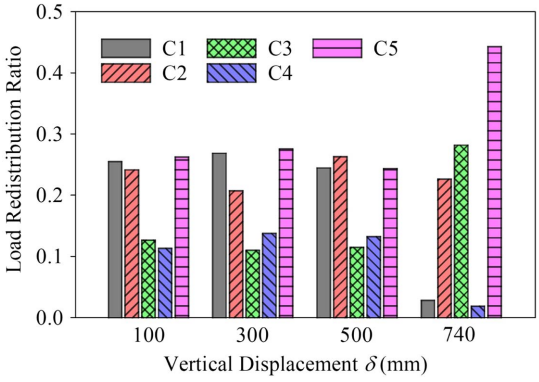

Fig. 30. Load redistribution ratio of each column.

column by the applied force. The load redistribution ratios in the columns are illustrated in Fig. 30. At the vertical displacement of 100 mm, the C1, C2, and C5 columns carried similar loads that consisted of a 75% portion of the total vertical load, while the C3 and C4 columns equally shared the rest. This distribution pattern was unchanged until the vertical displacement reached beyond 500 mm. At the vertical displacement of 740 mm, the load carried by the C1 column was transferred to the adjacent columns, e.g., C3 and C5, due to the failure at the G1-C1 connection. As shown in Fig. 15, the G1-C1 connection failure also caused a slight rotation of the load-distribution system around the actuator and the incline of the third-level distribution beam close to the C4 column. As a result, the load carried by the C4 column decreased.

Conclusions

In this paper, a 2×1 bay full-scale composite floor system was quasi-statically tested to failure under a middle-edge-column removal scenario. The primary objectives of the test were to investigate the load-resisting mechanisms and the quantified contribution percentages of the structural components to the resistance. The conclusions can be drawn as follows:

- The maximum resistance was achieved at a displacement of 686 mm (0.163 rad in the chord rotation angle), in which the contribution percentages of the steel girder and the composite slab were 19.2% and 80.8%, respectively. The combined resistance provided by the catenary action and the tensile membrane action was 15.9% higher than that by the flexural action alone.
- The static load-resisting capacity of the test specimen is 5.5 times that of the ASCE load combination for extraordinary events, while the dynamic load-resisting capacity is 4.1 times that of the ASCE load combination. After the complete rupture of the girder section, the floor system cannot achieve a higher resistance by relying on the composite slab membrane action.
- In the test, the membrane action could undergo a larger vertical displacement than the catenary action. Therefore, measures that could potentially improve the membrane action, such as increasing the thickness of the steel deck, increasing the slab reinforcement ratio, and applying more shear stud to the girders and beams, are desirable to enhance the collapse resistance of the composite floor system.
- The yield lines were developed in the composite slab, and the yield-line theory could reasonably predict the floor resistance at the flexural stage.
- Compared with the test results from the composite floor systems with a discontinuous steel deck and simple shear connections, the continuous steel deck and moment-resisting connections adopted in this test significantly improved the loading-carrying capacity and the deformation capacity of the floor system.

Data Availability Statement

All data, models, or code generated or used during the study are available from the corresponding author by request.

Acknowledgments

The research presented in this paper was sponsored by the State Key Laboratory of Diaster Reduction in Civil Engineering (Tongji University) through Grant No. SLDRCE19-A-03 and the Natural Science Foundation of China (NSFC) through Grant No. 51378380. Any opinions, findings, conclusions, and recommendations expressed in this paper are those of the authors and do not necessarily reflect the views of the sponsors.

References

AISC. 2010. *Specification for structural steel buildings*. AISC 360. Chicago: AISC.

Alashker, Y., and S. El-Tawil. 2011. "A design-oriented model for the collapse resistance of composite floors subjected to column loss." *J. Constr. Steel Res.* 67 (1): 84–92. https://doi.org/10.1016/j.jcsr.2010.07.008.

Alashker, Y., S. El-Tawil, and F. Sadek. 2010. "Progressive collapse resistance of steel-concrete composite floors." *J. Struct. Eng.* 136 (10): 1187–1196. https://doi.org/10.1061/(ASCE)ST.1943-541X.0000230.

Alashker, Y., H. Li, and S. El-Tawil. 2011. "Approximations in progressive collapse modeling." *J. Struct. Eng.* 137 (9): 914–924. https://doi.org/10.1061/(ASCE)ST.1943-541X.0000452.

ASCE. 2017. *Minimum design loads and associated criteria for buildings and other structures*. ASCE/SEI 7-16. Reston, VA: ASCE.

Bao, Y., J. A. Main, and S.-Y. Noh. 2017. "Evaluation of structural robustness against column loss: Methodology and application to RC frame buildings." *J. Struct. Eng.* 143 (8): 04017066. https://doi.org/10.1061/(ASCE)ST.1943-541X.0001795.

CEN (European Committee for Standardization). 2006. *Eurocode 1: Actions on structures, part 1-7: General actions—Accidental actions*. EN 1991-1-7. Brussels, Belgium: CEN.

Dat, P. X., and K. H. Tan. 2014. "Experimental response of beam-slab substructures subject to penultimate-external column removal." *J. Struct. Eng.* 141 (7): 04014170. https://doi.org/10.1061/(ASCE)ST.1943-541X.0001123.

DoD (Department of Defense). 2016. *Design of buildings to resist progressive collapse*. UFC 4-023-03. Washington, DC: DoD.

Elsanadedy, H. M., T. H. Almusallam, Y. R. Alharbi, Y. A. Al-Salloum, and H. Abbas. 2014. "Progressive collapse potential of a typical steel building due to blast attacks." *J. Constr. Steel Res.* 101 (Oct): 143–157. https://doi.org/10.1016/j.jcsr.2014.05.005.

Fu, Q. N., K. H. Tan, X. H. Zhou, and B. Yang. 2017. "Load-resisting mechanisms of 3D composite floor systems under internal column-removal scenario." *Eng. Struct.* 148 (Oct): 357–372. https://doi.org/10.1016/j.engstruct.2017.06.070.

GSA (General Services Administration). 2013. *Alternate path analysis & design guidelines for progressive collapse resistance*. Washington, DC: GSA.

Hadjioannou, M., S. Donahue, E. B. Williamson, and M. D. Engelhardt. 2018. "Large-scale experimental tests of composite steel floor systems subjected to column loss scenarios." *J. Struct. Eng.* 144 (2): 04017184. https://doi.org/10.1061/(ASCE)ST.1943-541X.0001929.

Hadjioannou, M., S. Donahue, E. B. Williamson, M. D. Engelhardt, B. Izzuddin, D. Nethercot, H. Zolghadrzadehjahromi, D. Stevens, K. Marchand, and M. Waggoner. 2013. "Experimental evaluation of floor slab contribution in mitigating progressive collapse of steel structures." In Vol. 134 of *Safety and Security Engineering V*, 615–626. Southampton, UK: WIT Press.

Harris, H. G., and G. Sabnis. 1999. *Structural modeling and experimental techniques*. 2nd ed. Boca Raton, FL: CRC Press.

Izzuddin, B. A., A. G. Vlassis, A. Y. Elghazouli, and D. A. Nethercot. 2008. "Progressive collapse of multi-storey buildings due to sudden column loss—Part I: Simplified assessment framework." *Eng. Struct.* 30 (5): 1308–1318. https://doi.org/10.1016/j.engstruct.2007.07.011.

Johnson, E. S., J. E. Meissner, and L. A. Fahnestock. 2015. "Experimental behavior of a half-scale steel concrete composite floor system subjected to column removal scenarios." *J. Struct. Eng.* 142 (2): 04015133. https://doi.org/10.1061/(ASCE)ST.1943-541X.0001398.

Johnson, R. P. 2004. *Composite structures of steel and concrete beams, slabs, columns, and frames for buildings*. Malden, MA: Blackwell Publishing.

Li, H. 2013. "Modeling, behavior and design of collapse resistant steel frame buildings." Ph.D. dissertation, Dept. of Civil and Environmental Engineering, Michigan Univ.

Li, H., X. Cai, L. Zhang, B. Zhang, and W. Wang. 2017. "Progressive collapse of steel moment-resisting frame subjected to loss of interior column: Experimental tests." *Eng. Struct.* 150 (Nov): 203–220. https://doi.org/10.1016/j.engstruct.2017.07.051.

Lim, N. S., K. H. Tan, and C. K. Lee. 2017. "Experimental studies of 3D RC substructures under exterior and corner column removal scenarios." *Eng. Struct.* 150 (Nov): 409–427. https://doi.org/10.1016/j.engstruct.2017.07.041.

Lu, X., K. Lin, Y. Li, H. Guan, P. Ren, and Y. Zhou. 2017. "Experimental investigation of RC beam-slab substructures against progressive collapse subject to an edge-column-removal scenario." *Eng. Struct.* 149 (Oct): 91–103. https://doi.org/10.1016/j.engstruct.2016.07.039.

Mitchell, D., and W. Cook. 1984. "Preventing progressive collapse of slab structures." *J. Struct. Eng.* 110 (7): 1513–1532. https://doi.org/10.1061/(ASCE)0733-9445(1984)110:7(1513).

MOHURD (Ministry of Housing and Urban-Rural Development of the People's Republic of China). 2003. *Code for design of steel structure*. GB50017. Beijing: MOHURD.

MOHURD (Ministry of Housing and Urban-Rural Development of the People's Republic of China). 2010. *Code for seismic design of buildings*. GB50011. Beijing: MOHURD.

Park, R., and W. L. Gamble. 2000. *Reinforced concrete slabs*. New York: Wiley.

Qian, K., and B. Li. 2012. "Slab effects on response of reinforced concrete substructures after loss of corner column." *ACI Struct. J.* 109 (6): 845.

Qian, K., and B. Li. 2015. "Load-resisting mechanism to mitigate progressive collapse of flat slab structures." *Mag. Concr. Res.* 67 (7): 349–363.

Qian, K., B. Li, and J. X. Ma. 2014. "Load-carrying mechanism to resist progressive collapse of RC buildings." *J. Struct. Eng.* 141 (2): 04014107. https://doi.org/10.1061/(ASCE)ST.1943-541X.0001046.

Qian, K., B. Li, and Z. Zhang. 2016. "Influence of multicolumn removal on the behavior of RC floors." *J. Struct. Eng.* 142 (5): 04016006. https://doi.org/10.1061/(ASCE)ST.1943-541X.0001461.

Sadek, F., S. El-Tawil, and H. Lew. 2008. "Robustness of composite floor systems with shear connections: Modeling, simulation, and evaluation." *J. Struct. Eng.* 134 (11): 1717–1725. https://doi.org/10.1061/(ASCE)0733-9445(2008)134:11(1717).

Sawczuk, A., and T. Jaeger. 1963. *Grenztragfähigkeits-Theorie der Platten*. Berlin: Springer-Verlag.

Starossek, U. 2009. *Progressive collapse of structures*. London: Thomas Telford.

Su, Y., Y. Tian, and X. Song. 2009. "Progressive collapse resistance of axially-restrained frame beams." *ACI Struct. J.* 106 (5): 600–607.

Wang, J., W. Wang, and X. Qian. 2019. "Progressive collapse simulation of the steel-concrete composite floor system considering ductile fracture of steel." *Eng. Struct.* 200 (Dec): 109701. https://doi.org/10.1016/j.engstruct.2019.109701.